International Journal of Nanomedicine

Dovepress
Taylor & Francis Group

Open Access Full Text Article

ORIGINAL RESEARCH

Glucose-Responsive Dual-Enzyme Mimetic Nanoreactor Remodels Diabetic Periodontitis Microenvironment for Augmented Alveolar Bone Regeneration

Dai Wang[1,*], Jianzhao Chen[1,*], Junjie Wang[2,*], Haojie Chen[1], Wenqiang Li[3], Shan Shen[2]

[1]School of Stomatology, Jinan University, Guangzhou, Guangdong, People's Republic of China; [2]Hospital of Stomatology, The First Affiliated Hospital of Jinan University, Guangzhou, Guangdong, People's Republic of China; [3]Guangdong Traditional Medical and Sports Injury Rehabilitation Research Institute, The Affiliated Guangdong Second Provincial General Hospital of Jinan University, Guangzhou, Guangdong, People's Republic of China

*These authors contributed equally to this work

Correspondence: Wenqiang Li, Guangdong Traditional Medical and Sports Injury Rehabilitation Research Institute, The Affiliated Guangdong Second Provincial General Hospital of Jinan University, Guangzhou, Guangdong, People's Republic of China, Email liwq@gzsport.edu.cn; Shan Shen, Hospital of Stomatology, The First Affiliated Hospital of Jinan University, Guangzhou, Guangdong, People's Republic of China, Email tshensh@jnu.edu.cn

Background: Periodontitis in the context of diabetes severely disrupts bone metabolic homeostasis, leading to irreversible alveolar bone loss. The resulting alveolar bone defects face significant challenges in healing due to a pathological microenvironment characterized by the interplay of hyperglycemia, oxidative stress, infection, and inflammation. Existing therapeutic strategies often lack the capability to synchronously and intelligently regulate this complex milieu, resulting in delayed and inefficient bone repair.

Methods: A composite material, termed MTS@QP-G@CO, was developed. Its core consists of manganese dioxide (MnO_2) nanoflowers loaded with a tannic acid (TA) -strontium metal (Sr)-phenolic network. These were conjugated with glucose oxidase via phenylboronic acid bonding and encapsulated within a pH-responsive Schiff base hydrogel. The structural characterization of the material, the performance of the cascade reaction, as well as its antioxidant and antibacterial properties have all been fully verified. A series of in vitro and in vivo experiments were conducted to evaluate the system's efficacy in modulating the local metabolic and oxidative status, inducing macrophage polarization, promoting osteogenic differentiation, and restoring bone regeneration in diabetic alveolar bone defect models.

Results: The MTS@QP-G@CO designed sequential action at the defect site involves triggering a "glucose starvation" effect via glucose oxidase, followed by hydrogen peroxide decomposition and oxygen generation catalyzed by the MnO_2 nanozyme. This achieves synchronized glucose reduction, hypoxia alleviation, reactive oxygen species (ROS) scavenging, and antibacterial activity. Subsequently, TA and Sr^{2+} are programmable released. And the system effectively remodeled the local pathological microenvironment in diabetic bone defects. It successfully achieved synchronized precise glucose reduction, hypoxia alleviation, ROS scavenging, and bacterial inhibition. This was followed by the cooperative release of therapeutic ions, which modulated the immune microenvironment by suppressing inflammation and inducing macrophage polarization toward the pro-healing M2 phenotype. Consequently, the system accelerated early osteogenic differentiation and bone matrix maturation, transforming the disordered repair process into a coordinated and efficient regeneration, leading to high-quality bone repair.

Conclusion: The MTS@QP-G@CO system effectively reverses the pathological microenvironment, coordinates immune modulation and osteogenesis, and transforms delayed healing into efficient, high-quality bone regeneration, offering a promising therapeutic approach for diabetes-related bone defects.

Keywords: cascade reaction, enzyme activity, macrophage polarization, osteogenic differentiation

https://doi.org/10.2147/IJN.S602215
Received: 8 February 2026
Accepted: 1 June 2026
Published: 5 June 2026

Graphical Abstract

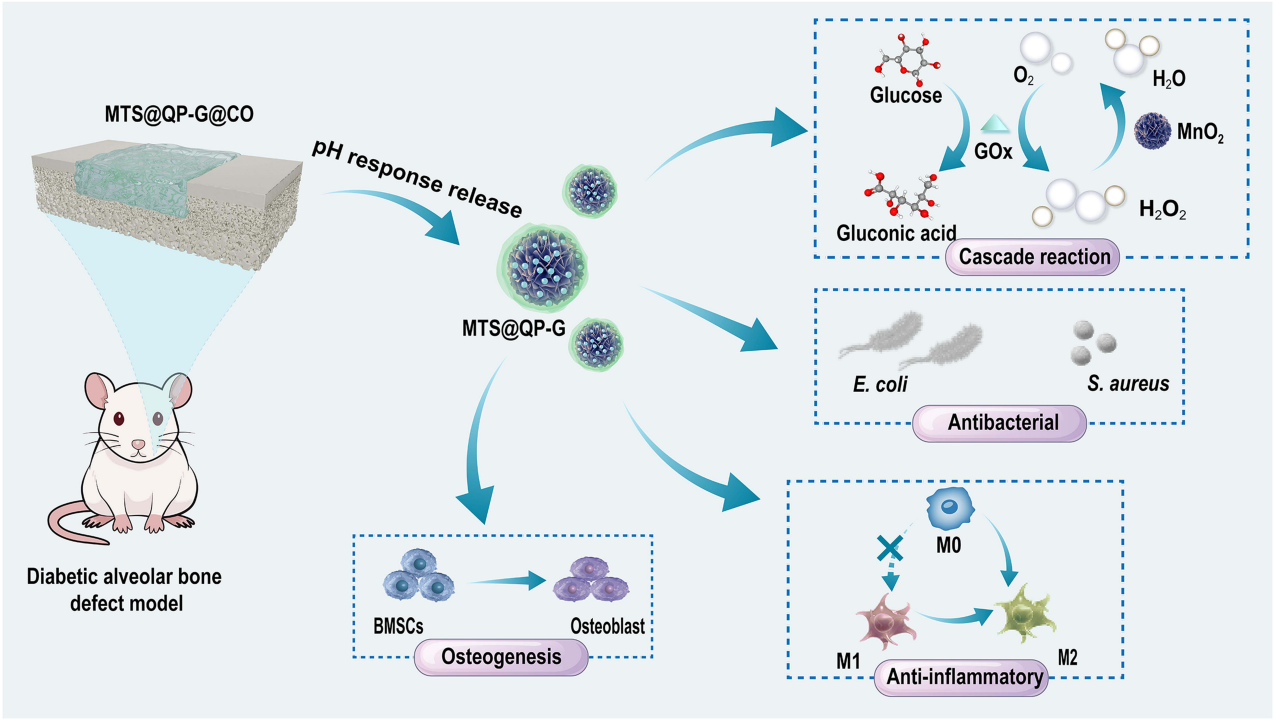

Introduction

Periodontitis is a chronic inflammatory disease induced by pathogenic plaque biofilm, with its core pathological feature being alveolar bone resorption under sustained inflammation, ultimately leading to tooth mobility and loss.[1,2] Notably, periodontitis is recognized as the "sixth major complication" of diabetes, forming a bidirectional and mutually reinforcing vicious cycle.[3,4] On one hand, the hyperglycemic state in diabetes not only provides nutrients for periodontal pathogens but also generates advanced glycation end products that persistently activate immune cells, triggering an excessive and destructive inflammatory response, thereby significantly exacerbating the severity and progression of periodontitis. On the other hand, as a chronic inflammatory focus, periodontitis releases inflammatory mediators into the systemic circulation, aggravating insulin resistance and impairing glycemic control, further complicating diabetes management.[5,6] In this mutually exacerbating pathological context, the occurrence of alveolar bone defects results directly from the combined action of multiple destructive factors. Diabetes-associated advanced glycation end products, oxidative stress, hyperglycemic toxicity, and local hypoxia synergize with chronic inflammation at the periodontal site, profoundly disrupting bone metabolic homeostasis.[7,8] This leads to abnormally enhanced osteoclast activity alongside severely impaired osteoblast function and survival, ultimately resulting in irreversible bone loss characterized by "excessive resorption over formation". Consequently, conventional periodontal therapies such as scaling and root planing, along with local antimicrobial approaches, may temporarily control infection but fail to fundamentally reverse the systemic inhibition of bone healing imposed by the diabetic microenvironment.[9,10] Therefore, developing a synergistic therapeutic strategy capable of simultaneously regulating local hyperglycemia, suppressing excessive immune inflammation, and directly promoting osteogenesis is particularly urgent and essential for achieving effective regeneration of diabetic alveolar bone defects.[11]

Hyperglycemia is a key pathological driver of diabetic alveolar bone defects, which can induce macrophage pyroptosis. This leads to the massive release of inflammatory cytokines and exacerbates periodontal tissue destruction.[12] While insulin serves as an effective systemic intervention for glycemic control, its long-term

administration may be associated with risks such as hypoglycemia, edema, and weight gain.[13] As a natural oxidoreductase, glucose oxidase (GOx) catalyzes the conversion of glucose to gluconic acid and hydrogen peroxide (H_2O_2), which underlies its use in localized "glucose starvation" therapy.[14,15] However, the direct application of GOx faces significant limitations: firstly, its catalytic process consumes oxygen, potentially aggravating pre-existing hypoxia in alveolar bone defect areas and promoting anaerobic bacterial proliferation; secondly, the product gluconic acid causes local pH reduction, exacerbating acidosis, inhibiting osteoblast activity, and activating osteoclasts; thirdly, the generated H_2O_2 further intensifies oxidative stress and directly damages osteoblasts.[13,16–18] Therefore, in an isolated system, the catalytic byproducts of GOx may exert multiple adverse effects on bone repair. The key challenge in constructing an efficient and intelligent diabetic alveolar bone regeneration system lies in ingeniously designing a delivery platform that circumvents these side effects and transforms its catalytic products into positive signals conducive to tissue regeneration.

In the treatment of diabetic bone defects, it is essential not only to regulate local hyperglycemia but also to concurrently intervene in the excessive and persistent inflammatory response and oxidative stress it triggers. This dual approach is a prerequisite for reversing the bone-destructive microenvironment and creating potential for tissue regeneration.[19,20] Natural enzyme-assisted therapeutic strategies have recently emerged as a promising approach for treating periodontitis and other diseases.[21] For instance, superoxide dismutase (SOD), catalase (CAT), and glutathione peroxidase (GPX) – key components of the cellular antioxidant defense system,[22] can scavenge reactive oxygen species (ROS) and alleviate oxidative stress. However, their practical application is severely limited by poor physiological stability, susceptibility to protease degradation, high production cost, and potential immunogenicity.[23,24] In contrast, nanozymes offer a robust alternative by mimicking the catalytic functions of SOD, CAT, and GPX, combining excellent stability with tunable activity. Nanomaterials such as manganese dioxide (MnO_2),[25] cerium oxide (CeO_2)[26] and ferrite (Fe_3O_4)[27] have been widely studied for mimicking the activities of SOD, CAT, and GPX, which underscores their significant potential in antioxidant applications.[28] In particular, nanozymes with catalase-like activity can decompose excessive H_2O_2 into H_2O and O_2, not only alleviating oxidative stress but also enabling a cascade reaction with glucose oxidase to convert harmful metabolic byproducts into beneficial signals for tissue repair.[29,30] Nevertheless, most current nanozymes still exhibit a relatively singular mechanism, primarily targeting specific ROS, which limits their ability to comprehensively regulate the complex inflammatory signaling pathways in diabetic bone defects.[31] Therefore, developing integrated strategies that go beyond simple catalytic activity and enable intelligent and synergistic regulation of the complex immune microenvironment has become a core challenge and urgent need in this field.

In response to the aforementioned challenges, this study designed and constructed a glucose-activated cascade nanozyme system (MTS@QP-G@CO) aimed at intelligently remodeling the microenvironment of diabetic alveolar bone defects and achieving efficient regeneration through spatiotemporally ordered cascade responses and multifunctional synergy. The system employs MnO_2 nanoflowers as the core carrier, which are first loaded with a tannic acid (TA)/strontium (Sr) metal-phenolic network (MTS) possessing antioxidant and osteogenic potential. Subsequently, the MTS nanoflowers are coated with a phenylboronic acid-modified quaternary ammonium chitosan layer (QP), and GOx is anchored to the surface via boronate ester bonds, forming intelligent nanoparticles (MTS@QP-G). Finally, MTS@QP-G nanoparticles are encapsulated within a pH-responsive oxidized sodium alginate (OSA)/carboxymethyl chitosan (CMCS)-based Schiff base hydrogel (CO), creating an integrated therapeutic platform (MTS@QP-G@CO). In a pathological microenvironment simulating diabetic alveolar bone defects, this system demonstrates a stepwise responsive therapeutic behavior: first, the acidic environment triggers hydrogel degradation, enabling controlled release of the nanoparticles. Next, the surface-bound glucose oxidase dissociates and diffuses under local high-glucose stimulation, achieving localized "glucose starvation" through catalytic glucose consumption while simultaneously producing acid and H_2O_2, thus establishing a preliminary antibacterial barrier; subsequently, the exposed MnO_2 nanoflowers exhibit catalase-like activity, efficiently decomposing the H_2O_2 generated by GOx into O_2 and H_2O, alleviating oxidative stress while improving local hypoxia and further inhibiting anaerobic bacterial survival; finally, the gradually released TA and Sr^{2+} synergistically exert anti-inflammatory effects, modulate the immune microenvironment, and directly promote osteogenic differentiation. In summary, the cascade nanozyme-hydrogel system developed in this study not only achieves multidimensional and synchronous intervention targeting the core pathological factors of diabetic alveolar bone defects (hyperglycemia, oxidative stress, hypoxia, infection, and inflammation) but also, through the temporal coordination

and spatial synergy of its functional components, transforms harmful metabolic byproducts into resources for tissue repair. Thereby, it actively reprograms the destructive microenvironment into a reparative one conducive to immune regulation and bone regeneration, offering novel insights and methodologies for the treatment of diabetes-related refractory bone defects (Figure 1).

Experimental Section

Materials

Tannic acid (TA, 98%), Strontium chloride hexahydrate ($SrCl_2.6H_2O$, 99.5%), 2-Formylphenylboronic acid (98%), Quaternary ammonium salt chitosan (degree of substitution: 92%), N-(3-Dimethylaminopropyl)-N′-ethylcarbodiimide (EDC, 95%), N-Hydroxysuccinimide(NHS, 98%), Glucose oxidase (GOx, Derived from Aspergillus niger, >180 U/mg), Sodium alginate (SA, 90%), Sodium periodate (99.5%), Carboxymethyl chitosan (degree of substitution: 80%), and

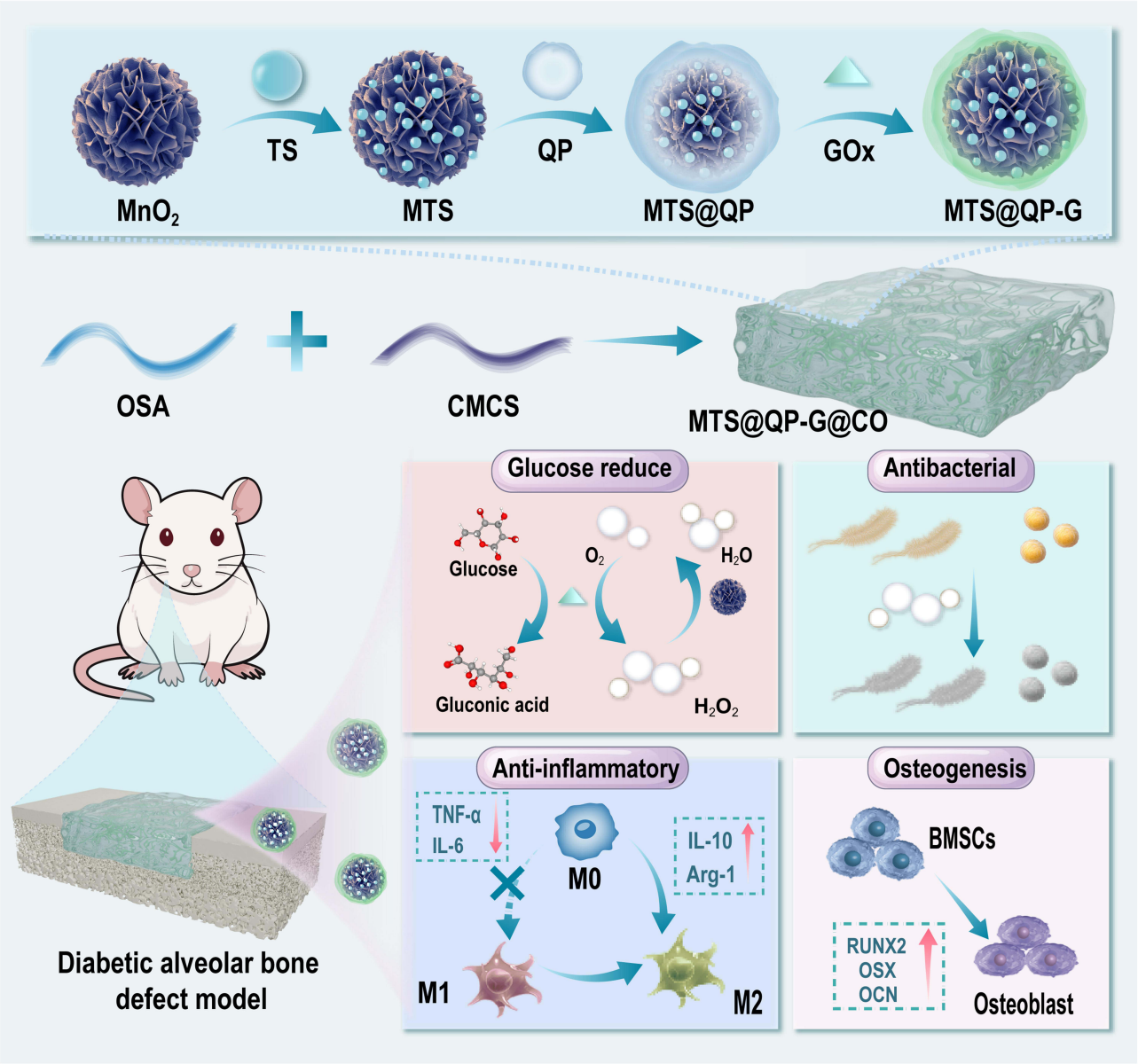

Figure 1 Schematic diagram of the synthesis of MTS@QP-G@CO hydrogel and its schematic diagram illustrating the cascading reactions for lowering blood sugar, generating oxygen, antibacterial, anti-inflammatory, and promoting bone formation (The red upward arrow indicates an increase in protein expression, while the red downward arrow indicates a decrease in protein expression).

https://doi.org/10.2147/IJN.S602215

D-(+)-Glucose (Glu, 99%) were purchased from Shanghai Macklin Biochemical Technology Co., Ltd. Potassium permanganate solution ($KMnO_4$, 98%) was purchased from Shanghai Aladdin Biochemical Technology Co., Ltd.

Synthesis and Characterization of MTS@QP-G Nanoparticles

MnO_2 nanoflowers were prepared by stirring a mixture of 50 mL 0.5 M $KMnO_4$ and 10 mL 4 M HCl at 80 °C for 30 min. After collection by centrifugation, the product was washed repeatedly with deionized water and ethanol, followed by drying at 80 °C.[32]

TS nanoparticles were synthesized by first dissolving 85 mg of tannic acid in 100 mL water with 10 min of vigorous stirring. Then, 40 mg of $SrCl_2 \cdot 6H_2O$ was added, the pH was adjusted to 8.0 with 1 M NaOH, and the mixture was stirred overnight. The resulting TA/Sr nanoparticles were collected by centrifugation (10,000 rpm, 5 min) and lyophilized.[33]

MTS nanoparticles were synthesized by dispersing 20 mg of TA/Sr nanoparticles (1 mg/mL) in 50 mL of water. After adding 30 mg of MnO_2, the mixture was stirred for 6 h. The product was then collected by centrifugation (5000 rpm, 5 min), washed twice with purified water, and lyophilized.

QP was synthesized by first activating 200 mg of 2-FPBA (in 20 mL water) with 720 mg EDC and 450 mg NHS via 30-min stirring. This solution was then added to 1 g of QCS dissolved in 50 mL water. The reaction mixture was stirred in the dark at room temperature for 24 h. The successful formation of QP was verified by nuclear magnetic resonance spectrometer (^{1}H NMR, BRUKER AVANCE 400, Germany).[34]

MTS@QP-G nanoparticles were prepared by incubating 50 mg MTS nanoparticles in 50 mL of QP solution (0.1 mg/mL) for 3 h. Following centrifugation and resuspension in 50 mL water, 20 mg GOx was introduced, and the mixture was stirred overnight in the dark at room temperature. The product was isolated via centrifugation, lyophilized, and the GOx loading was determined with a BCA assay.

Transmission electron microscopy (TEM, FEI Tecnai F20, USA) was employed to observe the morphology of MnO_2 nanoflowers, TS nanoparticles, MTS nanoparticles, and MTS@QP-G nanoparticles. Ultraviolet-visible spectrophotometry (UV-Vis, SHIMADZU UV 3600, Japan) was used to verify the successful loading of TA. X-ray photoelectron spectroscopy (XPS, Thermo Kalpha, USA) was applied to analyze the elemental valence states in the MTS@QP-G nanoparticles, while X-ray diffraction (XRD, ultima iv, UK) confirmed the crystal structures of the MnO_2 and MTS nanoparticles.

Encapsulation efficiency (EE) of TA, the characteristic absorption peaks of TA at 278 nm under different concentrations were measured using ultraviolet spectroscopy to establish a standard curve. The supernatant was retained during the preparation of TS and MTS. The concentration of TA was calculated based on the standard curve. And the EE was calculated according to the following formula (1).

$$\mathrm{EE} = (1 - \frac{C_S}{C_T}) \times 100\% \quad (1)$$

Among them, C_S represents the protein concentration in the supernatant after TA/GOx adsorption, and C_T represents the total protein concentration of the input.

The EE of GOx was determined using the BCA protein assay. A standard curve was first established with various concentrations of GOx. The protein concentrations of GOx before and after adsorption were then calculated from the standard curve, and the EE was calculated according to the following formula (1).

The peroxidase (POD)-mimicking activity of GOx was assessed as follows: a mixture containing 50 mM glucose (0.4 mL), 100 μM $FeCl_2$ (0.4 mL), and MTS@QP-G nanoparticles (2 mg/mL, 1 mL) was incubated for 30 minutes. Subsequently, 3,3′,5,5′-tetramethylbenzidine (TMB, 6 mM, 0.2 mL) was added, followed by centrifugation at 5000 rpm for 3 minutes. The absorbance of the supernatant was measured at 652 nm.

CAT-mimicking activity was evaluated using a salicylic acid assay and an H_2O_2 detection kit. For the former, nanoparticles (2 mg/mL, 0.2 mL) were incubated with Fe^{2+}, H_2O_2, and PBS for 30 min before adding salicylic acid and measuring absorbance at 510 nm. For the latter, nanoparticles were incubated with H_2O_2 and PBS for 10 min, then processed according to the kit protocol, with absorbance read at 405 nm.[35]

Synthesis and Characterization of MTS@QP-G@CO Hydrogels

OSA was synthesized by oxidizing SA. Briefly, 5 g SA was dissolved in 250 mL water, followed by the addition of 5.4 g sodium periodate. The reaction was carried out under N_2 in the dark at room temperature for 3 h. After adding 2.5 mL ethylene glycol to terminate the reaction and stirring for 1 h, the product was purified by dialysis (3500 Da, 2 days, with frequent water changes) and finally lyophilized.

The MTS@QP-G@CO hydrogel was prepared by mixing 5% (w/v) solutions of OSA and CMCS in equal volumes, and add a concentration of 0.1 wt% of MTS@QP-G. For morphological analysis, cross-sections of the lyophilized hydrogel (obtained by fracturing in liquid nitrogen) were gold-coated and examined by scanning electron microscopy (SEM, Sigma 300, Germany). Its mechanical properties were assessed via compression tests on cylindrical samples (15 mm × 10 mm) using a universal testing machine at 10 mm/min.

Drug Release

To determine the loading capacity of TA, first prepare a standard curve by measuring the absorbance at 278 nm of a series of TA standard solutions using a mixed solvent of 0.1 M ascorbic acid and 0.1 M HCl. Then, digest the nanoparticles with the same mixed solution. Finally, calculate the TA loading capacity according to Formula (2) below:

$$\text{Drugloadingcapacity} = \frac{ThemassofTA}{Themassofnanoparticles} \tag{2}$$

To assess the drug release profile, 0.5 g of the MTS@QP-G@CO hydrogel was incubated in 10 mL of three different media: PBS at pH 7.4, PBS at pH 6.0, and PBS at pH 6.0 with 10 mM glucose. The supernatant collected by centrifugation at specified time points was analyzed by UV-Vis spectrophotometry. The absorbance at 278 nm was used to determine the cumulative release ratio of TA.

Degradation Experiment

The freeze-dried hydrogels were respectively immersed in PBS (pH 7.4) medium. They were incubated at 37 °C and 100 rpm shaker for different time points. After removing the materials at different time points, they were freeze-dried, and the mass was measured to calculate the mass degradation ratio.

Antioxidant Experiment

The radical scavenging activity was evaluated using DPPH and $ABTS^{\cdot+}$ assays. For DPPH, samples (200 μL of nanoparticles at 1 mg/mL or 0.2 g hydrogel) were incubated with 1800 μL of 0.2 mM DPPH (in ethanol) for 30 min, followed by absorbance measurement at 517 nm. The $ABTS^{\cdot+}$ assay was performed analogously, with a working solution prepared from ABTS and potassium persulfate, and using ascorbic acid (VC) as a positive control. The scavenging ratios for both assays were calculated using the standard formula (3):

$$\text{DPPH/ABTS scavenging ratio} = \frac{A_N - A_S}{A_N - A_P} \times 100\% \tag{3}$$

A_N, A_S, and A_P denote the absorbance of the negative control, test sample, and positive control, respectively.

Antibacterial Experiment

To evaluate antibacterial activity, 0.5 g samples of CO, MTS@QP-G@CO, and MTS@QP-G@CO+Glu hydrogels were co-cultured with 1 mL bacterial suspensions (with 400 μL of 500 mg/mL glucose added to the last group). Growth curves for *Escherichia coli* (*E. coli*) and *Staphylococcus aureus* (*S. aureus*) were obtained by OD measurement. After 8 h, 100 μL of the culture was serially diluted (10^6-fold), plated on agar, and incubated overnight at 37 °C for colony enumeration.

For SEM observation of bacterial morphology, control and material-treated bacterial suspensions were first centrifuged, PBS-washed, and dropped onto silicon wafers. After air-drying, the samples were fixed overnight with glutaraldehyde, dehydrated in an ethanol gradient, dried, gold-coated, and finally imaged by SEM.

To quantify biofilm formation, bacterial suspensions (OD600 = 0.1) were first co-incubated with materials for 8 h. Subsequently, 100 μL aliquots were transferred to 24-well plates with fresh LB medium and incubated statically for 48 h. After PBS washing, biofilms were fixed with methanol, air-dried, stained with 0.1% crystal violet, washed again, and the dye was eluted with 95% ethanol. Absorbance was finally measured at 570 nm.

Biocompatibility Test

Disinfect 1 g of CO and the MTS@QP-G@CO hydrogel under UV light for 30 minutes, then immerse them in 10 mL of serum-free α MEM medium. Incubate the mixture at 37 °C, shaking gently for 24 h. After incubation, collect the supernatant, centrifuge it at 3000 rpm for 10 minutes. Then add 10% fetal bovine serum and 1% penicillin/streptomycin to the obtained extract.

To evaluate biocompatibility, cells were seeded into 96-well plates at a density of 5×10^3 cells per well and subsequently exposed to 100 μL of material extract. Following 24 or 48 hours of incubation, cell viability was assessed via live/dead staining using calcein-AM and PI. Metabolic activity was determined using the CCK-8 assay (measuring absorbance at 450 nm). For morphological evaluation, after 24 h of co-culture, cells were fixed, permeabilized, blocked, and then stained with rhodamine-phalloidine and DAPI. Imaging was performed using confocal microscopy, and the spreading area was quantified through ImageJ-based analysis.

For the Transwell experiment, cell migration was evaluated using 24-well Transwell chambers (8.0 μm pore size). BMSCs were first subjected to serum starvation for 12 h, then seeded into the upper chamber at a density of 2×10^4 cells per well in 200 μL of serum-free medium. The lower chamber was filled with 600 μL of complete medium containing 10% FBS, serving as a chemoattractant. After 24 h of incubation, cells that had migrated to the underside of the membrane were fixed with 4% paraformaldehyde, stained with 0.1% crystal violet for 15 min, and finally visualized and imaged under a light microscope.

Hemolysis test: Hydrogel (200 μL) was mixed with 1.5 mL of a 2% (v/v) red blood cell (RBC) suspension, and the mixture was incubated at 37 °C for 3 h. Saline and deionized water were used as negative and positive controls, respectively. Following centrifugation at 3000 rpm for 5 min, the absorbance of the supernatant was measured at 540 nm.

Measurement of the Inflammatory Microenvironment Regulated by MTS@QP-G@CO Hydrogel in vitro

Establishment of high-glucose/hypoxia model: BMSCs were seeded into culture plates. After cell attachment, the medium was replaced with high-glucose DMEM (glucose concentration: 25 mM) and cultured under hypoxic conditions. Hypoxia was maintained in a dedicated tri-gas incubator with oxygen concentration set at 1%–3%, CO_2 at 5%, and temperature at 37 °C. Cell proliferation and viability under model conditions were assessed using live/dead staining and the CCK-8 assay.

To detect intracellular ROS levels, cells and 100 μL material extract were treated under high-glucose/hypoxic conditions, then incubated with 10 μM DCFH-DA in serum-free medium at 37 °C for 30 min (dark). After PBS washing, fluorescence microscopy was used for observation.

Immunofluorescence staining of HIF-1α: Cells grown in confocal dishes were exposed to high-glucose/hypoxic conditions for 12 h. Afterwards, they were fixed using 4% paraformaldehyde, permeabilized with 0.5% Triton X-100, and blocked with 5% BSA. A primary antibody against HIF-1α was applied overnight at 4 °C, followed by a 1-h incubation at room temperature with a fluorescent secondary antibody (protected from light). Nuclear counterstaining was performed with DAPI. The expression level and nuclear translocation of HIF-1α were assessed under a fluorescence microscope, based on the intensity and distribution pattern of green fluorescence signals.

Macrophage Polarization: Cells were treated with medium containing lipopolysaccharide (LPS, 100 ng/mL) for 24 h to induce M1-type polarization. For immunofluorescence, after fixation, permeabilization, and blocking, cells were stained with primary antibodies against CD86 and CD206, followed by corresponding fluorescent secondary antibodies. Nuclei were counterstained with DAPI, and the expression and distribution of M1/M2 phenotype markers were observed under a confocal fluorescence microscope. For flow cytometry analysis, cells were harvested after treatment, directly

stained with fluorescently labeled anti-CD86 and anti-CD206 antibodies for surface markers, washed, resuspended, and analyzed on a flow cytometer to determine the percentage of positive cells.

Determination of in vitro Osteogenic Differentiation Ability

Alkaline phosphatase (ALP) staining for early osteogenic differentiation: After 7 days of osteogenic induction, cells were fixed and incubated with BCIP/NBT substrate to develop an insoluble purple precipitate. Representative fields were imaged under an optical microscope. Alizarin Red S (ARS) staining for late mineralization nodule formation: Following 21 days of induction, cells were fixed and stained with ARS solution. After thorough washing, red/orange-red calcium nodules were observed and imaged under a microscope for qualitative and semi-quantitative analysis. For quantitative real-time polymerase chain reaction (qPCR) to precisely quantify osteogenic gene expression, total RNA was extracted from cells using TRIzol reagent after 14 days of induction. cDNA was synthesized using the HiScript III 1st Strand cDNA Synthesis Kit (Vazyme, Nanjing, China) with 200 ng of total RNA as template. The remaining reagents and amplification procedures followed the manufacturer's instructions, and the resulting cDNA was directly used for subsequent qPCR. The forward and reverse primer sequences for the target genes are listed in Table S1. GAPDH was used as the housekeeping gene for normalization, and relative quantification was performed using the $2^{-}\Delta\Delta Ct$ method.

Construction and Evaluation of an in vivo Model of Diabetic Alveolar Bone Defect

All animal welfare procedures followed the Chinese National Standard GB/T 35892–2018 "Guideline for Welfare and Ethical Review of Laboratory Animal" and were approved by the Laboratory Animal Welfare and Ethics Committee of Jinan University (Approval Number: IACUC-20251202-03). The study reporting followed the ARRIVE guidelines. Male Sprague-Dawley rats weighing approximately 250 g were used for the in vivo experiments. To establish a diabetic rat model, streptozotocin (STZ) was administered as a single intraperitoneal injection at a dose of 50 mg/kg body weight (2% wt/vol solution). Blood glucose levels were measured at 72 h and one week after injection. Animals with random blood glucose ≥16.7 mmol/L were considered successfully modeled. After 24 h of fasting, rats were anesthetized with 3% sodium pentobarbital (30 mg/kg). The surgical site was disinfected with iodine, and a 1 cm incision was made at the mesial aspect of the maxillary first molar to expose the alveolar bone. A bone defect measuring approximately 3.0×2.0 × 1.0 mm (length × width × depth) was created using a dental handpiece with sequential drilling. According to the experimental groups, 10 μL of hydrogel was injected into the defect. After gelation, the full-thickness flap was sutured intermittently with 5-0 absorbable sutures. Rats received an intramuscular injection of 80,000 units of penicillin into the hind leg and were placed on a heating pad until recovery. At 4 weeks post-treatment, rats were euthanized using a CO_2 chamber. Rats were placed into the sealed chamber, and CO_2 was introduced until respiratory arrest was confirmed, followed by an additional 1-minute gas flow to prevent accidental recovery. Death was confirmed by the absence of heartbeat and respiration, along with obvious cyanosis of the paws and tail. Tissue samples were collected and evaluated by micro-computed tomography (Micro-CT) to assess healing of the alveolar bone defect. Histological analyses including hematoxylin and eosin (H&E) staining, Masson's trichrome staining, immunofluorescence staining for CD31 and RUNX2, and immunohistochemical staining for type-I collagen (Col-I) and osteocalcin (OCN) were performed to comprehensively evaluate bone repair.

Statistical Analysis

Image-derived data were quantified with ImageJ and Origin, reported as mean ± SD. Statistical significance across groups was determined by one-way ANOVA, with p-values indicated as $*p < 0.05$, $**p < 0.01$, $***p < 0.001$.

Results and Discussion

Design and Characterization of MTS@QP-G Nanoparticles with Dual Enzymatic Activity

MnO_2 nanoparticles were prepared via $KMnO_4$ reduction method. SEM characterization revealed that the obtained product exhibited a sea urchin-like nanoflower structure with a diameter of approximately 500 nm (Figure 2a). Under

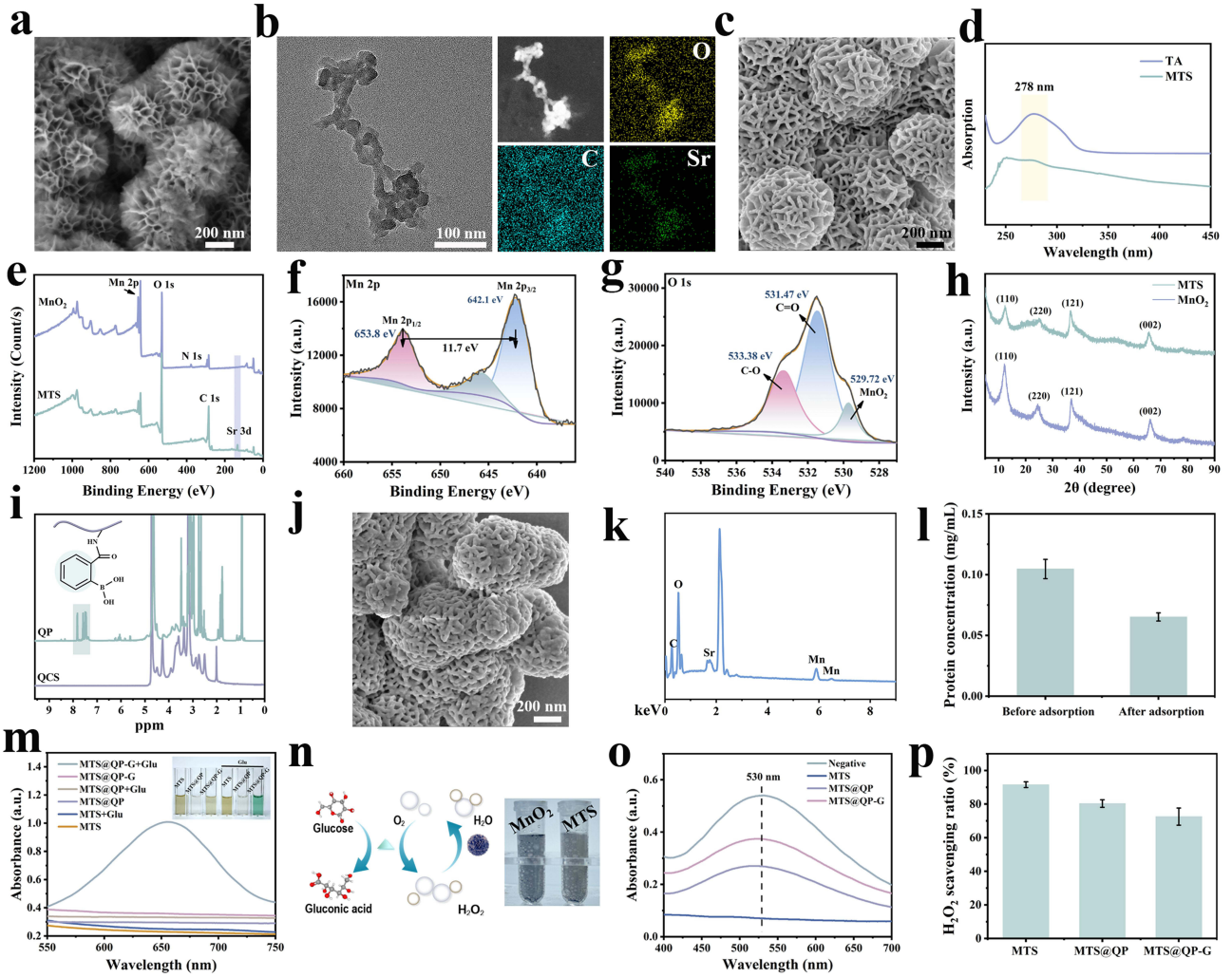

Figure 2 (**a**) SEM image of MnO_2. (**b**) TEM image and mapping elemental analysis of TS nanoparticles. (**c**) SEM image of MTS. (**d**) UV spectroscopy analysis of TA and MTS. (**e**) Total elemental XPS spectrum of MnO_2 and MTS. The XPS detailed spectrum of MTS: (**f**) Mn 2p and (**g**) O1s. (**h**) XPS spectrum of MnO_2 and MTS. (**i**) ^{1}H NMR spectrums of QP and QCS. (**j**) SEM image of MTS@QP-G and (**k**) EDS analysis. (**l**) Quantitative statistics before and after GOx adsorption. (**m**) Verification of the enzymatic activity of GOx in MTS@QP-G using the TMB method. (**n**) MTS@QP-Cascade reaction schematic diagram and the physical image of oxygen production through CAT enzyme activity. (**o**) Verification of the ability of MTS. MTS@QP and MTS@QP-G nanoparticles to scavenge H_2O_2 using the salicylic acid method. (**p**) Quantitative statistics of H_2O_2 scavenging ratios of MTS.MTS@QP and MTS@QP-G nanoparticles.

alkaline conditions, spherical metal-phenolic nanoparticles with a size of about 20 nm were successfully synthesized through the deprotonation of TA and its coordination with Sr^{2+}. The elemental mapping clearly demonstrated the uniform distribution of Sr, C, and O, confirming the formation of TS nanoparticles (Figure 2b). After loading the TS nanoparticles onto the manganese dioxide nanoflowers, SEM and TEM images showed uniform embedding of the TS nanoparticles within the nanoflower structure (Figure 2c and S1). The UV-visible absorption spectrum exhibited a characteristic absorption peak at 278 nm attributed to TA, indicating successful loading of TS (Figure 2d). XPS full scan confirmed the presence of strontium in the MTS composite material (Figure 2e). After calibration using the C 1s binding energy at 284.8 eV as a reference (Figure S2a), the Mn 2p spectrum displayed two characteristic peaks at 642.1 eV and 653.8 eV, corresponding to Mn $2p_{3/2}$ and Mn $2p_{1/2}$, respectively, indicating that manganese predominantly existed in the +4 oxidation state (Figure 2f).[32] The O 1s spectrum could be deconvoluted into three peaks: at 529.7 eV attributed to the Mn-O-Mn bond, and at 531.5 eV and 533.4 eV assigned to the C=O and C-O-H bonds in TA, respectively (Figure 2g). Additionally, the Sr 3d spectrum showed the Sr $3d_{5/2}$ binding energy at 133.8 eV, further confirming the formation of a metal-phenolic coordination network (Figure S2b).[36] X-ray diffraction patterns further verified the crystalline structures of both MnO_2 and the MTS composite material (Figure 2h). Furthermore, based on the calibration curve (Figure S3), the

https://doi.org/10.2147/IJN.S602215

load efficiency (EE) of TA was calculated to be 55.54%. To achieve spatiotemporally matched treatment for the pathological process of diabetic alveolar bone defects, phenylboronic acid-modified quaternary ammonium chitosan was synthesized. The ^{1}H NMR spectrum displayed characteristic peaks for the phenyl protons of phenylboronic acid in the chemical shift range of 7–8 ppm, confirming the successful synthesis of QP (Figure 2i). After coating the MTS nanoparticles with the QP layer and conjugating GOx via boronate ester bonds, SEM and EDS confirmed the successful preparation of MTS@QP-G nanoparticles (Figure 2j and k). Based on the BCA protein quantification standard curve (Figure S4), the loading efficiency of glucose oxidase was calculated to be 37.69% (Figure 2l). The nano-particle structure was disrupted by using acid digestion, thereby releasing TA for the measurement of the drug loading capacity of TA as 16 μg/mg (Figure S5).

Subsequently, the dual-enzyme catalytic activity of the MTS@QP-G nanoparticles was systematically evaluated. Firstly, the GOx activity was verified using the TMB method: H_2O_2 generated by GOx-catalyzed glucose oxidation decomposes in the presence of Fe^{2+} to produce hydroxyl radicals (·OH), which then oxidize colorless TMB into a blue product, generating a characteristic absorption peak at 652 nm. As shown in Figure 2m, only when glucose was added to the MTS@QP-G system did the solution turn blue and exhibit a characteristic absorption peak, indicating that the GOx embedded in the nanoparticles retained efficient glucose catalytic capability. A schematic diagram illustrating the cascade reaction mechanism of the nanoparticles is presented in Figure 2n, wherein the MnO_2 core mimics catalase activity, decomposing H_2O_2 into oxygen and water. This catalytic activity was further confirmed using the salicylic acid method, where ·OH generated via Fe^{2+}-catalyzed decomposition of H_2O_2 reacts with salicylic acid to produce a characteristic absorption peak at 510 nm. Upon addition of MTS nanoparticles, this absorption peak was significantly diminished (Figure 2o), demonstrating their efficient H_2O_2 scavenging ability. Quantitative analysis using an H_2O_2 detection kit confirmed that the H_2O_2 scavenging rate of the MTS nanoparticles reached 91.57 ± 1.72% (Figure 2p). In summary, the above characterization results confirm that the MTS@QP-G nanoparticles were not only successfully constructed but also effectively exhibited dual catalytic functions of glucose oxidase and catalase, laying the material foundation for subsequent cascade reactions and microenvironment modulation.

Design and Characterization of MTS@QP-G@GO Hydrogel

To address the acidic microenvironment of diabetic alveolar bone defects, this study designed and prepared a pH-responsive hydrogel (CO hydrogel) based on the Schiff base reaction, aiming to precisely fill irregular bone defect areas. The hydrogel employs OSA as the aldehyde donor. The ^{1}H NMR spectrum of OSA exhibited a characteristic peak for the aldehyde proton at 5.30 ppm (Figure 3a), and the FT-IR spectrum showed a newly formed aldehyde characteristic absorption peak at 1729 cm^{-1} (Figure 3b), collectively confirming the successful synthesis of OSA.[37] Subsequently, the aldehyde groups of OSA and the amino groups of CMCS cross-linked via the Schiff base reaction to form the hydrogel. The FT-IR spectrum revealed the disappearance of the aldehyde characteristic peak after the reaction (Figure 3c). Furthermore, the absorption peak of the -NH_2 group in CMCS at 3403 cm^{-1} shifted to 3299 cm^{-1} due to the formation of imine bonds (-NH-), confirming the successful construction of the hydrogel (a schematic of the gelation process is shown in Figure 3d). SEM demonstrated that the internal network structure of the nanoparticle-loaded hydrogel (MTS@QP-G@CO) became denser with reduced pore size compared to the pure CO hydrogel (Figure 3e and f), and the MTS@QP-G nanoparticles are uniformly distributed within the hydrogel matrix (Figure S6a and b), indicating that the introduction of nanoparticles increased the physical cross-linking points. Mechanical property tests revealed that the compressive strength of the CO hydrogel correlated with the OSA/CMCS ratio, with the 1:1 ratio exhibiting optimal performance (Figure 3g). Upon nanoparticle loading, the mechanical properties of the MTS@QP-G@CO hydrogel were further enhanced (Figure 3h), which is consistent with the structural changes observed via SEM.

Furthermore, the release behavior of TA from the hydrogel exhibited environmental responsiveness (Figure 3i). In simulated diabetic microenvironmental conditions, specifically acidic (pH 6.0) and high- Glu (10 mM Glu) media, the TA release ratio was significantly higher than that under physiological neutral conditions (pH 7.4). Notably, in pH 6.0 PBS supplemented with 10 mM Glu, the cumulative release of TA reached 77.47 ± 1.82% after 80 h. This enhanced release can be attributed to the accelerated swelling and degradation of the hydrogel network under acidic conditions, coupled with glucose competition that promotes boronate ester bond cleavage and dissociation of the QP coating, thereby

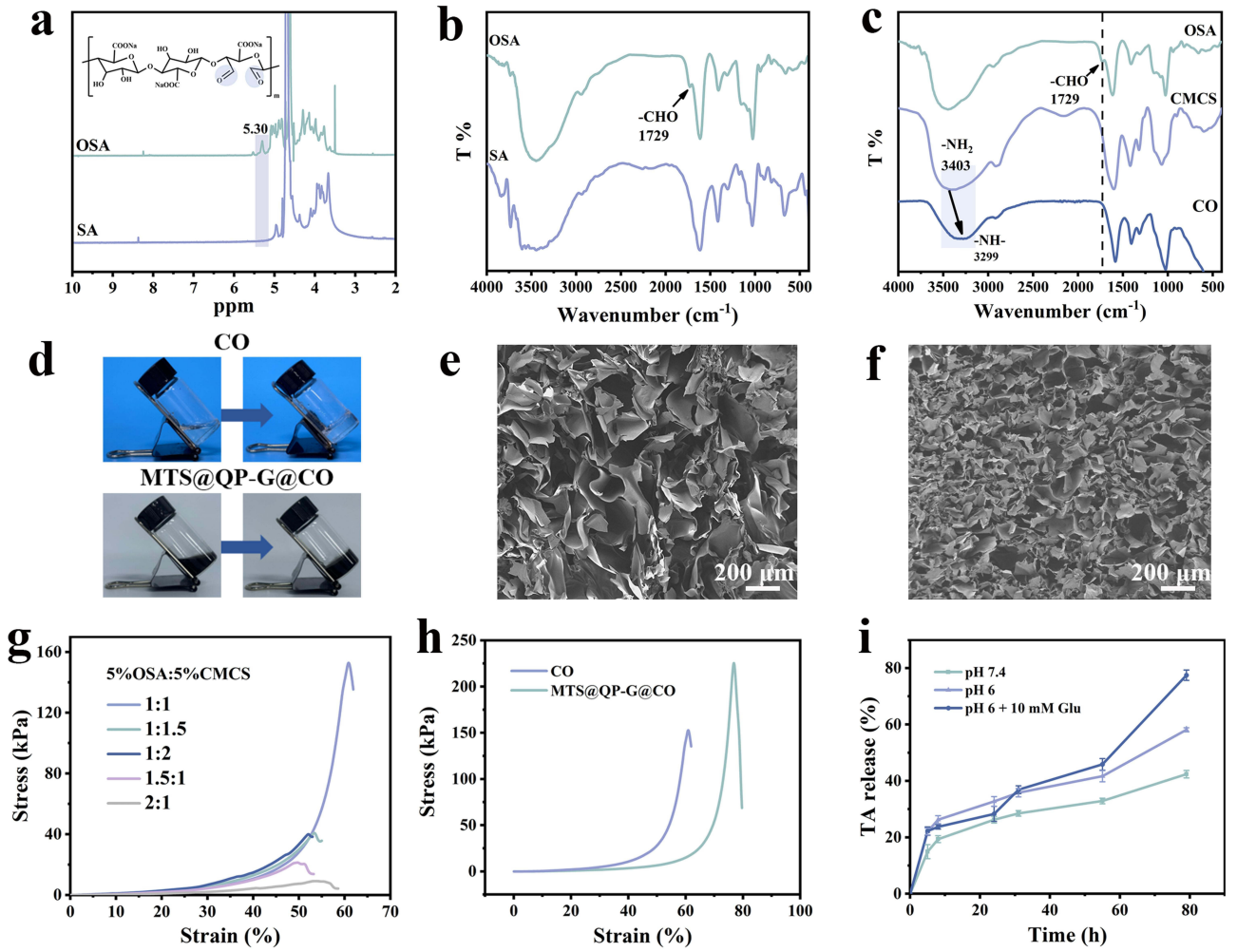

Figure 3 (**a**) ^{1}H NMR spectrums of SA and OSA. (**b**) FT-IR spectrums of SA and OSA. (**c**) FT-IR spectrums of OSA, CMCS and CO. (**d**) The physical image of the CO and MTS@QP-G@CO hydrogels after gelation. SEM images of (**e**) CO and (**f**) MTS@QP-G@CO hydrogels. (**g**) The stress-strain curves of CO hydrogels formed by different proportions of OSA and CMCS. (**h**) The stress-strain curves of CO and MTS@QP-G@CO hydrogels. (**i**) The release ratio of TA from MTS@QP-G@CO hydrogel in different media.

enabling intelligent and rapid drug release. In summary, this study successfully developed an intelligent hydrogel delivery system (MTS@QP-G@CO) with dual pH/Glu responsiveness. This system not only adapts to the morphology of irregular bone defects and provides appropriate mechanical support, but also precisely senses the pathological microenvironment (acidic and hyperglycemic) of diabetic alveolar bone defects, thereby driving the temporally controlled release of therapeutic agents. This platform represents a highly promising local treatment strategy for alveolar bone regeneration under diabetic conditions. The hydrogel was subjected to degradation experiments in PBS (pH 7.4) media. The results show that the hydrogel with a degradation ratio of 43.69 ± 0.96% on the 14th day (Figure S7). For alveolar bone regeneration, this moderate degradation ratio is desirable, it ensures sufficient scaffold stability during the initial healing phase, while progressively degrading to accommodate new bone ingrowth.

Evaluation of the ROS Scavenging and Antibacterial Capabilities of MTS@QP-G@CO Hydrogels

The pathological microenvironment of diabetic alveolar bone defects involves multiple ROS. The MTS@QP-G@CO hydrogel constructed in this study aims to address this challenge through synergistic mechanisms. To evaluate the antioxidant capacity, DPPH and $ABTS^{\cdot+}$ assays were performed. The results indicated that MTS nanoparticles possessed the optimal DPPH radical scavenging effect, with a scavenging ratio of 53.85 ± 2.09%, which was consistent with the

https://doi.org/10.2147/IJN.S602215

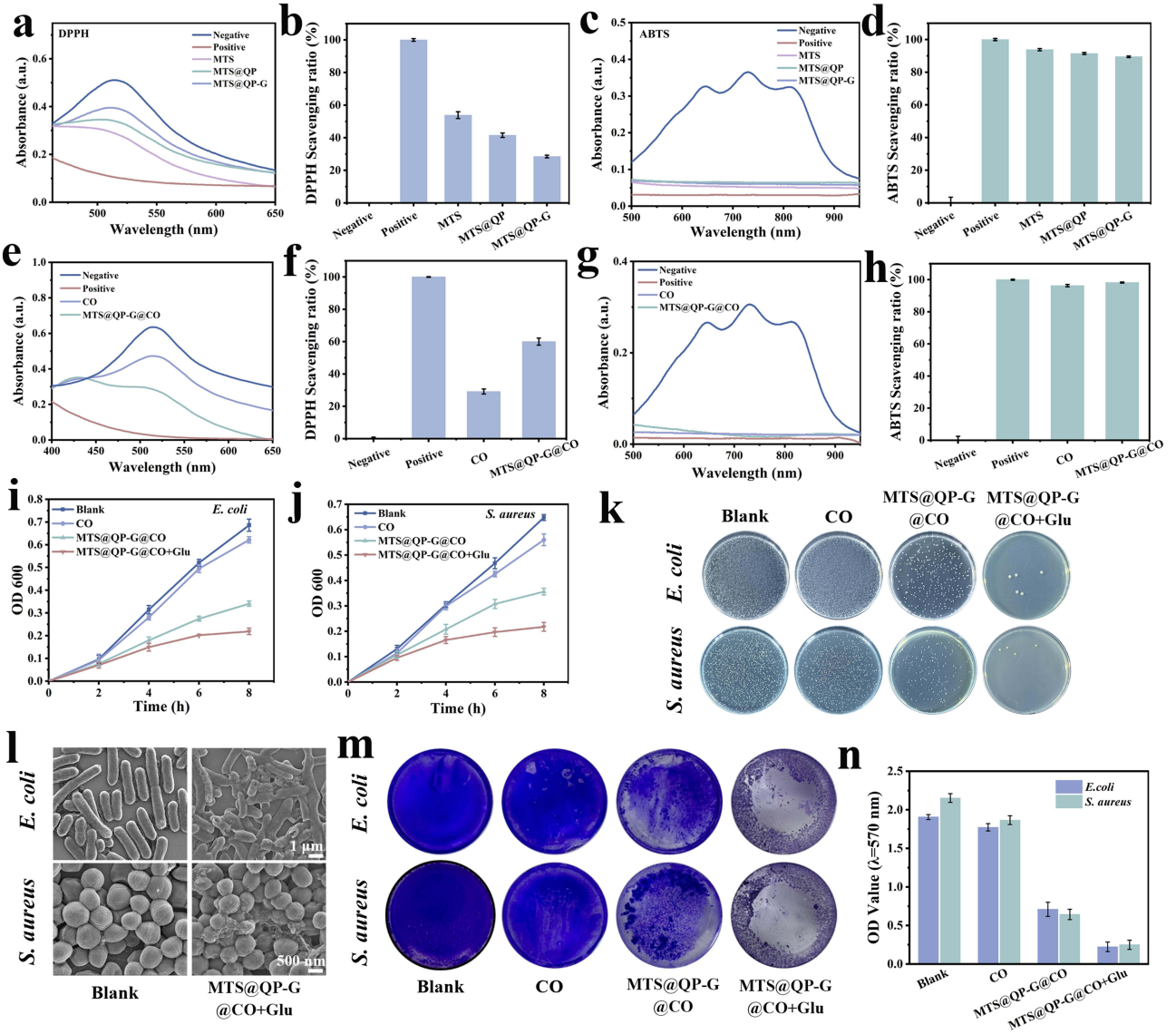

Figure 4 (**a**) UV absorption curves of DPPH by treated with MTS, MTS@QP and MTS@QP-G. (**b**) The DPPH radical scavenging ratios of MTS, MTS@QP and MTS@QP-G. (**c**) UV absorption curves of $ABTS^{\cdot+}$ by treated with MTS, MTS@QP and MTS@QP-G. (**d**) The $ABTS^{\cdot+}$ radical scavenging ratios of CO and MTS@QP-G@CO hydrogels. (**e**) UV absorption curves of DPPH by treated with CO and MTS@QP-G@CO hydrogels. (**f**) The DPPH radical scavenging ratios of CO and MTS@QP-G@CO hydrogels. (**g**) UV absorption curves of $ABTS^{\cdot+}$ by treated with MTS, MTS@QP and MTS@QP-G. (**h**) The $ABTS^{\cdot+}$ radical scavenging ratios of CO and MTS@QP-G@CO hydrogels. (**i** and **j**) The bacterial growth curves of CO, MTS@QP-G@CO and MTS@QP-G@CO + Glu groups after different durations of treatment compared with *E. coli* and *S. aureus*. (**k**) Images of bacterial colony. (**l**) SEM bacterial electron microscope images after treatment with PBS and MTS@QP-G@CO + Glu. (**m**) Physical images of crystal violet-stained biological membranes after different material treatments and (**n**) Determination of OD value after crystal violet staining.

attenuation of the characteristic absorption peak at 510 nm (Figure 4a and b). In the $ABTS^{\cdot+}$ assay, the characteristic absorption peak at 734 nm in the MTS group was nearly abolished, with a scavenging ratio as high as 93.79 ± 0.69% (Figure 4c and d), further confirming its potent radical scavenging capability. To evaluate the antioxidant performance of the final hydrogel system, the same radical scavenging assays were conducted. As shown in Figure 4e and f, the pure CO hydrogel exhibited only weak antioxidant activity, whereas the nanoparticle-loaded MTS@QP-G@CO hydrogel demonstrated significantly enhanced DPPH scavenging ability due to its nano-components. The $ABTS^{\cdot+}$ assay followed a similar trend (Figure 4g and h), confirming that the introduction of nanoparticles is the primary source of the hydrogel's antioxidant function. In summary, within this integrated system, the MTS@QP-G@CO hydrogel exerts comprehensive antioxidant effects through a dual-mechanism synergy: MnO_2 efficiently scavenges H_2O_2 generated by GOx catalysis and accumulated in the microenvironment, thereby reducing the production of highly toxic radicals (eg, ·OH) at the

 https://doi.org/10.2147/IJN.S602215

source. Simultaneously, TA acts as a broad-spectrum scavenger, directly quenching various residual radicals such as DPPH and $ABTS^{\cdot+}$. These two mechanisms work in concert to achieve systematic intervention in the oxidative stress microenvironment of diabetic bone defects.[38]

Diabetes significantly increases the susceptibility to and severity of periodontal bacterial infections. Therefore, conferring effective antibacterial properties to the repair materials is crucial for diabetic alveolar bone defects. This study evaluated the antibacterial capacity of the hydrogels. CO, MTS@QP-G@CO, and MTS@QP-G@CO+Glu groups were co-incubated with *E. coli* and *S. aureus*, and growth curves were plotted by monitoring the OD value of the bacterial suspensions (Figure 4i and j). The results showed that the MTS@QP@CO group itself exhibited certain antibacterial effects, and its efficacy was significantly enhanced in the presence of glucose. Further colony counting on agar plates visually demonstrated that after 6 hours of treatment with MTS@QP-G@CO+Glu, colony formation for both bacterial strains was almost completely inhibited (Figure 4k). SEM revealed the bactericidal mechanism: bacteria treated with MTS@QP-G@CO+Glu exhibited severe cell membrane/wall shrinkage, dissolution, and cytoplasmic leakage (Figure 4l). Considering the tendency for persistent biofilm formation in diabetic alveolar bone defect areas, the inhibitory effect of the materials on biofilms was also evaluated. Crystal violet staining showed that the biofilm structure in the control group remained intact, whereas the MTS@QP-G@CO+Glu group effectively inhibited biofilm formation (Figure 4m). Quantitative analysis confirmed that this group had the lowest absorbance for crystal violet, indicating significant removal of biofilm biomass (Figure 4n). In clinical practice, minocycline hydrochloride is commonly used to inhibit bacterial growth in the oral cavity. Studies have shown that it can achieve an inhibition ratio of over 75% against *S. aureus* biofilm formation.[39] In comparison, our MTS@QP-G@CO + Glu group exhibited a strong potential to prevent or reduce biofilm formation. The above results consistently demonstrate that MTS@QP-G@CO possesses robust antibacterial and anti-biofilm capabilities when triggered by glucose. The mechanism primarily stems from the continuous generation of high concentrations of H_2O_2 by the GOx on the material surface in the presence of glucose. H_2O_2 not only exhibits strong oxidative properties that directly damage key bacterial components such as proteins, lipids, and DNA, but also, in the presence of local trace metal ions (eg, Fe^{2+}), can be converted into the more potent ·OH through Fenton-like reactions, thereby achieving efficient clearance of both planktonic bacteria and biofilms. Additionally, the continuous consumption of local glucose by GOx reduces the nutrient source necessary for bacterial proliferation, further suppressing the development of infection at its source.[40]

Evaluation of the in vitro ROS Scavenging Ability of MTS@QP-G@CO

BMSCs were co-cultured with CO hydrogel and MTS@QP-G@CO hydrogel for 24 h and 48 h to systematically evaluate their biocompatibility. Both live/dead cell staining and CCK-8 assay results indicated that, compared to the Control group, cell viability in the CO and MTS@QP-G@CO hydrogel groups showed no significant difference (Figure 5a and b), demonstrating the absence of apparent cytotoxicity. Cytoskeleton staining revealed that cells in all groups exhibited favorable spreading, displaying typical spindle-shaped or triangular cytoskeletal morphology (Figure 5c). Quantitative analysis further indicated no statistically significant differences in cell spreading area among the three groups (Figure 5d). Transwell assays indicated a significantly higher density of migrated BMSCs in the CO and MTS@QP-G@CO hydrogel groups than in the Control (Figure 5e). Furthermore, the superior biosafety of the MTS@QP-G@CO hydrogel was further confirmed by hemolysis assay, which showed a hemolysis ratio of 1.74 ± 1.58%, well within the safe range (Figure S8). In summary, the MTS@QP-G@CO hydrogel combines excellent biocompatibility with the ability to promote cell migration.

To validate the ability of MTS@QP-G@CO to remodel the diabetic microenvironment, this study established a high-glucose and hypoxia cell model. As shown in Figure 5g, a significant number of dead cells was observed in the live/dead staining of the Model group, indicating successful model construction. In contrast, the MTS@QP-G@CO group exhibited a marked reduction in dead cells and a clear improvement in cell viability. CCK-8 assay further demonstrated that cell viability in this group recovered to over 80% (Figure 5f). Given that the high-glucose and hypoxia model induces oxidative damage, detection using the DCFH-DA probe revealed a sharp increase in ROS levels in the Model group (Figure 5h). In comparison, ROS expression was significantly reduced in the MTS@QP-G@CO group. Additionally, the HIF-1α protein, which typically accumulates under hypoxic conditions, also showed a decreasing

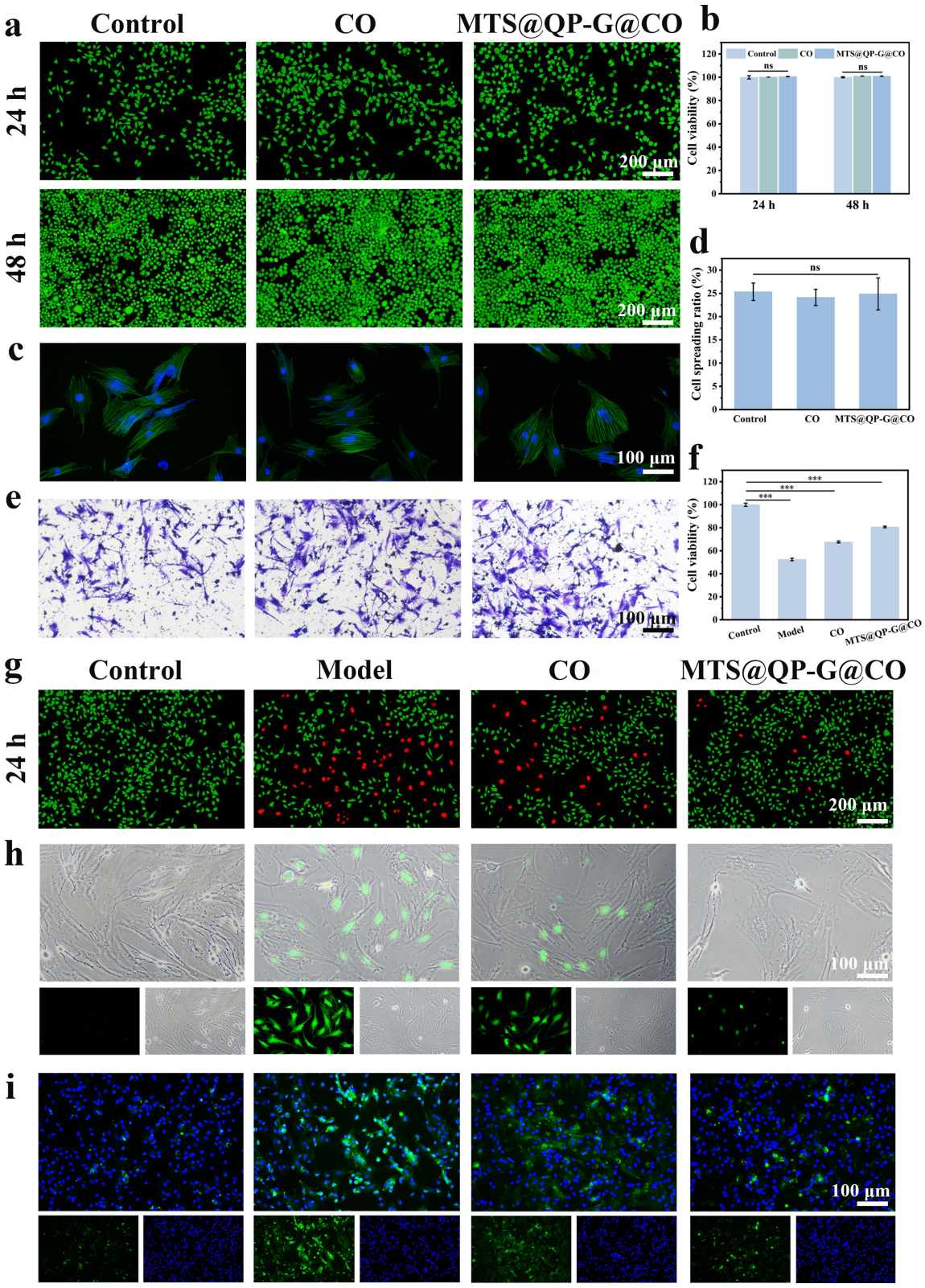

Figure 5 (**a**) Cell staining of live/dead cells was performed at 24 h and 48 h, and (**b**) CCK8 assay was used to determine cell viability. (**c**) Quantitative analysis of cytoskeleton staining and (**d**) cell spreading ratio. (**e**) Transwell experiment. (**f**) CCK8 assay was used to determine cell viability and (**g**) cell staining for live/dead cells in the hypoxic/high glucose model was conducted at 24 hours of incubation. (**h**) DCFH-DA staining in the hypoxic/high glucose model. (**i**) HIF-1α staining in the hypoxic/high glucose model. Significance levels of ***$p<0.001$ were applied. "ns" indicates that there is no significant difference among the groups.

https://doi.org/10.2147/IJN.S602215

trend in this group, indicating alleviation of the hypoxic state (Figure 5i). The excellent ROS scavenging and hypoxia-alleviating capabilities of MTS@QP-G@CO stem from its cascade reaction design. Firstly, GOx efficiently consumes Glu, and the by-product H_2O_2 is subsequently catalyzed by the CAT-mimicking activity of MnO_2 in the material, converting it into H_2O and O_2, thereby directly mitigating local hypoxia. Simultaneously, the released TA can further scavenge various forms of ROS in the microenvironment. This synergistic action significantly ameliorates the stress microenvironment induced by high glucose and hypoxia, creating favorable conditions for subsequent bone regeneration.

Evaluation of in vitro Macrophage Reprogramming and Osteogenic Function of MTS@QP-G@CO

The amelioration of the microenvironment directly influences the polarization state of macrophages. To simulate the inflammatory response under pathological conditions, this study utilized LPS to induce the polarization of macrophages from the M0 phenotype toward the pro-inflammatory M1 phenotype. Immunofluorescence staining results (Figure 6a) revealed a significant enhancement in the fluorescence signal of the M1 marker CD86 in the Model group, while expression of the M2 marker CD206 remained weak, confirming the successful establishment of the inflammatory polarization model. In the Control group, both markers exhibited low expression. Following intervention with the MTS@QP-G@CO hydrogel, the expression of CD86 was markedly reduced, while that of CD206 was significantly increased (Figure 6b and c). The hydrogel effectively induced a shift from M1 to M2 macrophage polarization, as demonstrated by flow cytometry (Figure 6d). Consistent with this phenotypic change, ELISA analysis showed a significant reduction in pro-inflammatory factors (TNF-α, IL-6) and an elevation in anti-inflammatory markers (IL-10, Arg-1) (Figure 6e, $***p < 0.001$). These consistent results indicate that the MTS@QP-G@CO hydrogel can effectively modulate macrophage polarization and remodel the inflammatory cytokine profile by improving the high-glucose, hypoxic microenvironment and releasing anti-inflammatory components such as TA, thereby exerting anti-inflammatory effects.[41]

To evaluate the osteogenic differentiation-inducing capability of the material, this study analyzed early differentiation and late mineralization levels through ALP activity assays and ARS staining, respectively. In an inflammatory model established using LPS-induced BMSCs, ALP activity at day 7 (Figure 6f) revealed that the ALP activity in the Model group was significantly suppressed, whereas treatment with the MTS@QP-G@CO hydrogel notably restored and enhanced ALP activity. ARS staining results at day 21 (Figure 6g) further demonstrated that the hydrogel-treated group exhibited significantly more calcium nodule deposition (red complexes) compared to the model group, confirming its ability to effectively promote late-stage mineralization. To further investigate the underlying molecular mechanisms, the expression of osteogenesis-related genes was examined via RT-PCR. As shown in Figure 6h, after 14 days of hydrogel treatment, mRNA expression levels of early transcription factors (RUNX2 and OSX) and late markers (OCN) in BMSCs were significantly upregulated, even surpassing those in the normal Control group. This indicates that the hydrogel not only reverses inflammation-induced suppression but also actively activates the osteogenic differentiation program. In summary, the osteogenic-promoting effect of the MTS@QP-G@CO hydrogel stems from a dual mechanism: on one hand, it indirectly ameliorates the inflammatory microenvironment by inducing macrophage polarization toward the M2 phenotype, thereby helping BMSCs regain normal function; on the other hand, the released strontium ions can directly activate osteogenic signaling pathways in the cells, thus more efficiently and directly initiating and accelerating the osteogenic differentiation process.[42,43]

Evaluation of Treatment for Diabetic Alveolar Bone Defects

The MTS@QP-G@CO hydrogel significantly enhanced alveolar bone regeneration in diabetic rats. In this model (STZ-induced, blood glucose ≥16.7 mmol/L), defects (3.0×2.0×1.0 mm) treated with MTS@QP-G@CO showed substantial new bone filling by Micro-CT at 4 weeks, unlike the PBS-treated Control which exhibited large voids (Figure 7a). Quantitative analysis confirmed superior bone microarchitecture in the MTS@QP-G@CO group, with significantly increased BV, BV/TV, BMD, Tb. N, Tb. Th and decreased Tb. Sp (Figure 7b–g). Clinically, rhBMP-2 is a standard osteoinductive agent for bone defect repair, yet it yields a BV/TV of only 40% and a BMD of 550 mg/cm^3. In contrast,

 https://doi.org/10.2147/IJN.S602215

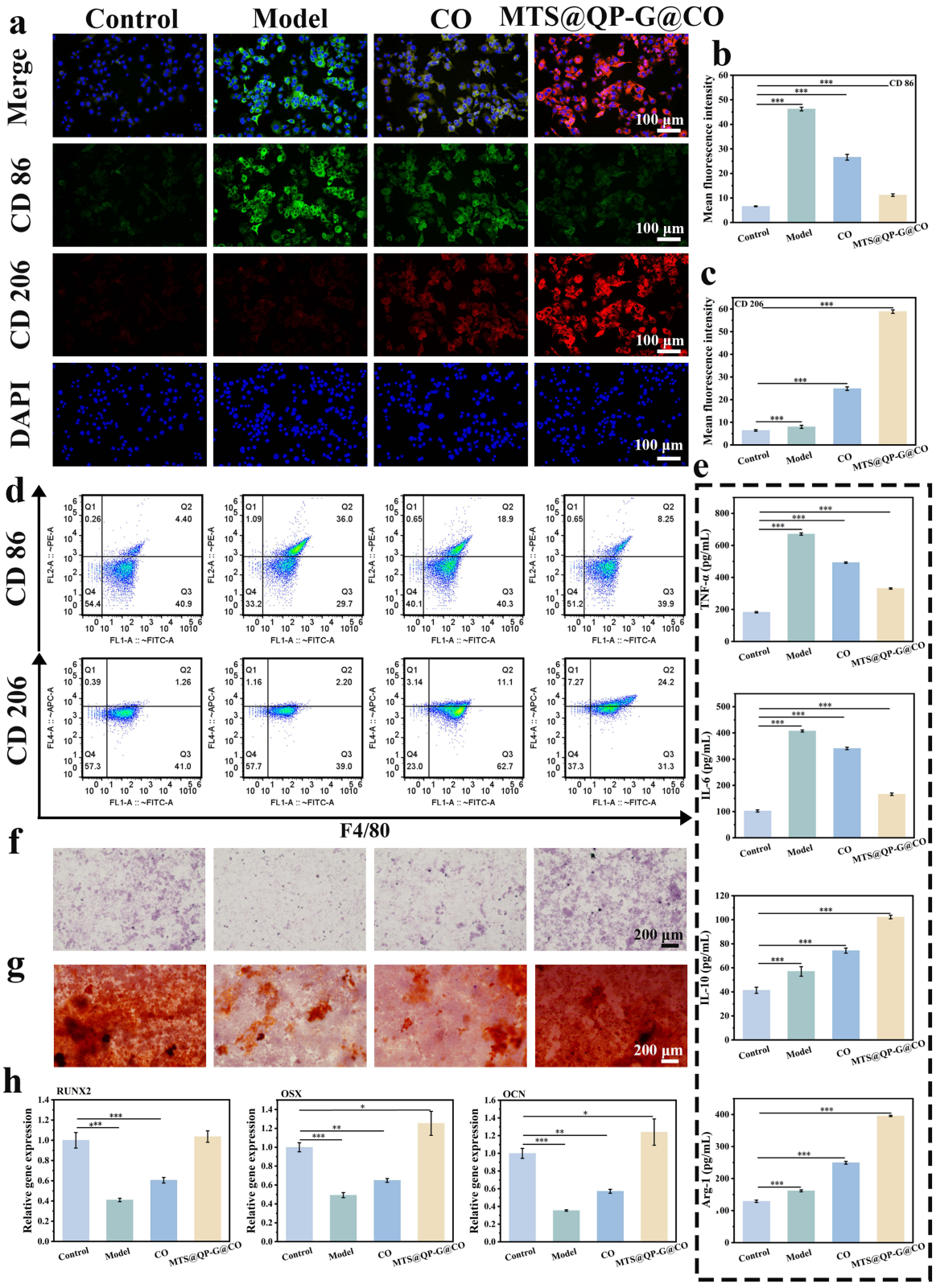

Figure 6 (**a**) Immunofluorescence staining of CD86-type and CD206-type macrophages and (**b** and **c**) mean fluorescence intensity quantification. (**d**) Flow cytometry analysis of the expression of CD86 and CD206. (**e**) Expression of inflammatory-related proteins by Elisa. (**f**) ALP staining. (**g**) ARS staining. (**h**) RT-qPCR was used to determine the expression of osteogenesis-related genes. Significance levels of *p< 0.05, **p< 0.01, and ***p<0.001 were applied.

https://doi.org/10.2147/IJN.S602215

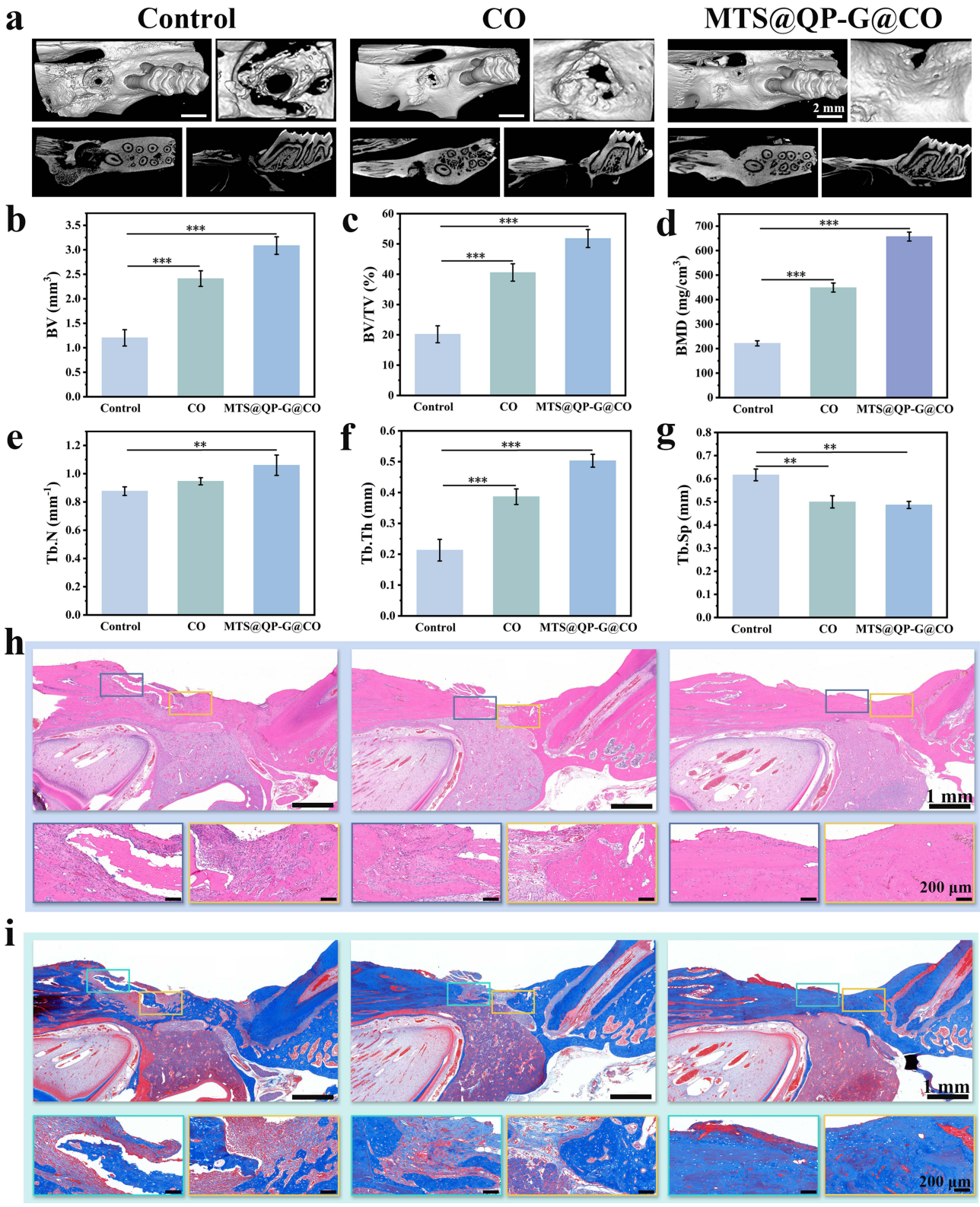

Figure 7 (**a**) Representative micro-CT images of alveolar bone defect model at 4 weeks. (**b–g**) Statistics of bone-related indicators: BV, BV/TV, BMD, Tb.N, Tb.Th and Tb.Sp. (**h**) H&E and (**i**) Masson staining representation of the image and its magnified local view (20X). Significance levels of $^{**}p < 0.01$, and $^{***}p < 0.001$ were applied.

https://doi.org/10.2147/IJN.S602215

the MTS@QP-G@CO group achieved significantly higher values than those of rhBMP-2.[44] In addition, scaling and root planing (SRP) can eliminate the initiators of inflammation by physically removing plaque biofilm and dental calculus, yet its ability to promote alveolar bone regeneration is limited. Studies have shown that, compared with the Control group, the SRP group increased the BV/TV by only approximately 3%,[45] whereas the MTS@QP-G@CO group achieved a 30% increase, demonstrating a remarkable capacity for alveolar bone repair. Histological evaluation was performed using H&E and Masson staining (Figure 7h and i). In the Control group, evident bone defects, significant inflammatory cell infiltration, and typical woven bone characteristics were observed. Masson staining revealed extensive red and red-blue intermixed areas, indicating a predominance of immature collagen. Conversely, H&E staining of the MTS@QP-G@CO group showed uniform tissue staining with no obvious inflammatory cell infiltration, while Masson staining demonstrated mature and orderly arranged blue collagen fibers, exhibiting characteristics of mature lamellar bone. These in vivo experimental results are consistent with the conclusions drawn from in vitro studies, indicating that the MTS@QP-G nanoparticles effectively promote high-quality bone regeneration through their multifaceted actions, including rapid blood glucose reduction, antibacterial activity, and anti-inflammatory effects.

Evaluation of Vascularization and Osteogenesis in Diabetic Alveolar Bone Defects

To elucidate the repair process of diabetic alveolar bone defects at the molecular and cellular levels, we further conducted immunofluorescence and immunohistochemical analyses. As shown in Figure 8a, positive CD31 fluorescence signals were scarcely detectable in the Control group, indicating that the hyperglycemic environment severely inhibited angiogenesis. In contrast, the MTS@QP-G@CO group exhibited clear signals of a nascent vascular network, suggesting effective improvement of blood supply in the defect area. Figure 8b results demonstrated that the expression of the transcription factor RUNX2, a marker for early-stage osteogenic differentiation initiation, remained distinctly evident in the Control group at week 4, while its fluorescence signal was significantly diminished in the MTS@QP-G@CO group. This pattern aligns with the dynamic expression profile of RUNX2 as an early-stage marker, indicating that the osteogenic process in the treatment group progressed more rapidly, having advanced beyond the differentiation initiation phase strongly dependent on RUNX2 and entered the subsequent matrix maturation stage. Immunohistochemical analysis further revealed the status of matrix synthesis and mineralization (Figure 8c and d). In the Control group, the positive staining area for Col-1 was small and diffuse, indicating insufficient and disorganized collagen matrix synthesis. Concurrently, OCN signals appeared discontinuous, abnormally localized, and diffuse, suggesting severely impaired and inefficient mineralization. Notably, the OCN signal intensity in the MTS@QP-G@CO group was lower than that in the Control group. Considering its superior morphological bone regeneration outcomes, we infer that this does not indicate insufficient mineralization but rather reflects an accelerated healing process in the treatment group. By week 4, the treatment group may have already progressed beyond the peak phase of rapid mineralization (characterized by high OCN expression) and entered the stage of new bone maturation and remodeling. Consequently, the number of osteoblasts actively secreting OCN has physiologically decreased, leading to a decline in signal intensity. In contrast, the healing process in the Control group was severely delayed, remaining stuck in an inefficient and disorganized state of active mineralization. This results in a persistently elevated, yet ineffective, OCN signal.

In summary, through multi-dimensional analyses including micro-CT, histomorphometry (H&E and Masson staining), and molecular markers (CD31, RUNX2, Col-1, OCN), this study systematically validates the superior reparative efficacy of MTS@QP-G@CO for diabetic alveolar bone defects. Its mechanism of action unfolds as a coordinated and accelerated cascade process: first, it creates a favorable systemic and local microenvironment for regeneration by rapidly lowering blood glucose and exerting anti-inflammatory effects; next, it significantly promotes angiogenesis, addressing the fundamental issue of ischemia; subsequently, the enhanced blood supply efficiently activates early-stage osteogenic differentiation; the activated osteoblasts then synthesize substantial, well-organized bone matrix and swiftly achieve high-quality mineralization (evidenced by an earlier OCN expression peak), ultimately forming lamellar bone with high mineral density and mature structure. The physiological decline in OCN signal in the treatment group at week 4, contrasting sharply with the persistently high pathological expression in the control group, precisely demonstrates from a kinetic perspective that MTS@QP-G@CO successfully transforms the delayed and low-quality bone healing under diabetic conditions into a rapid, high-quality, and physiological regeneration process. This study provides

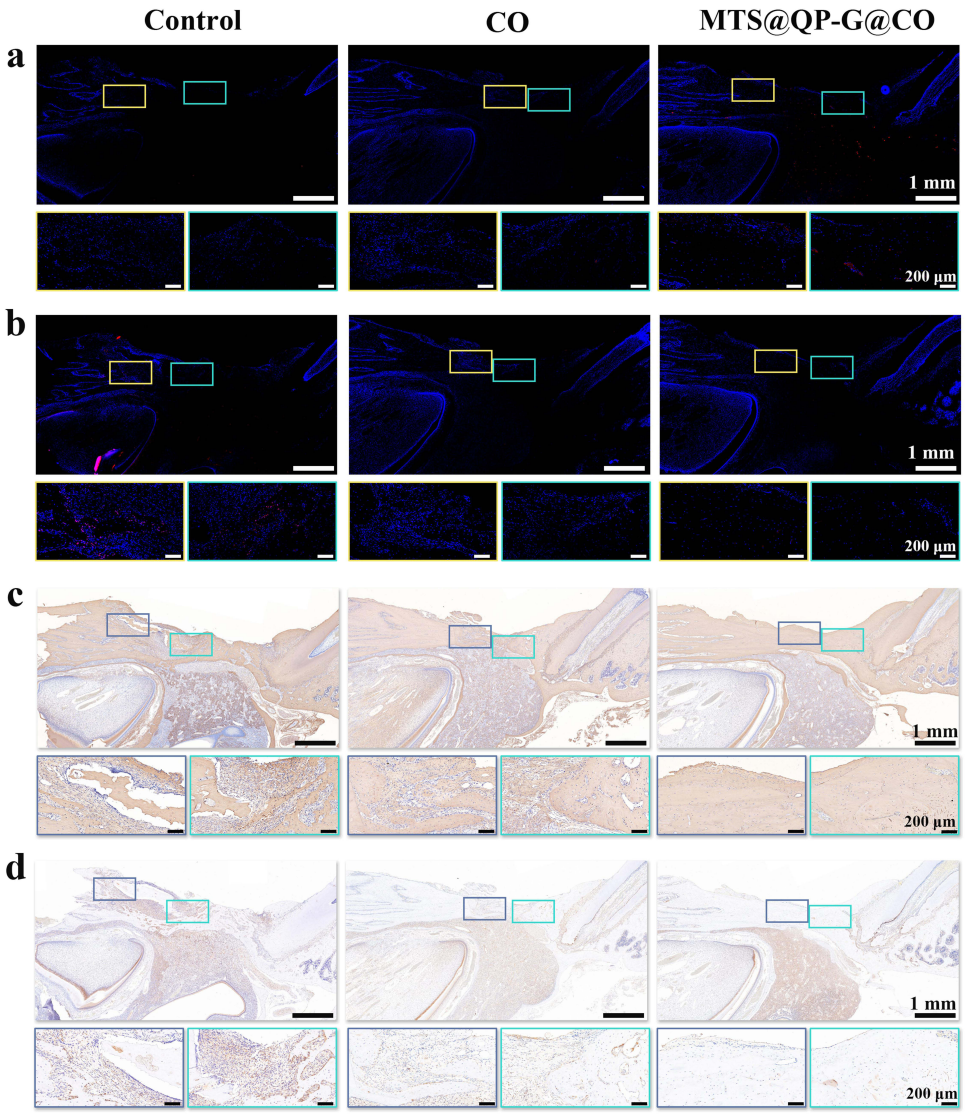

Figure 8 Immunofluorescence staining of (**a**) CD31 and (**b**) RUNX2. Immunohistochemical analysis of (**c**) Col-I and (**d**) OCN.

a multifunctional therapeutic strategy for maxillofacial bone regeneration in diabetes, integrating metabolic regulation, anti-inflammatory activity, pro-angiogenesis, and osteogenic promotion.

Conclusion

This study developed an intelligent composite material, MTS@QP-G@CO, featuring a glucose-responsive dual-enzyme cascade reaction for microenvironment modulation and regenerative repair of diabetic alveolar bone defects. By integrating boronate ester bond-responsive glucose oxidase with catalase-like MnO_2 nanozymes in a cascade, and combining it with a tannic acid-strontium metal-phenolic network, the material achieves controlled release within a pH-responsive hydrogel. This design enables synchronous local glucose reduction, oxygen generation, antioxidant, anti-inflammatory, and antibacterial functions. In diabetic bone defects, the material exerts a synergistic therapeutic effect by rapidly improving the local metabolic and oxidative milieu, promoting angiogenesis and osteogenic differentiation, and polarizing macrophages to a repair-supportive state, which collectively restores the compromised vascular-osteogenic coupling. Ultimately, this system transforms the delayed and low-quality bone healing associated with diabetes into a coordinated, high-quality regenerative process, advancing bone repair from the active mineralization phase into the

https://doi.org/10.2147/IJN.S602215

mature remodeling stage earlier. This research provides a multi-target synergistic microenvironment remodeling strategy for diabetic bone defects.

Data Sharing Statement

Data will be made available on request from corresponding author.

Funding

This work was project supported by the Research Project of Traditional Chinese Medicine Bureau of Guangdong Provincial (20201079), Guangzhou Basic and Applied Basic Research Foundation (2025A04J5261), and National Natural Science Foundation of China (32300962).

Disclosure

The authors declare no competing interest.

References

1. Lu J, Yu N, Zhang X, Wu Y, Fan D, Zhen L. Injectable thermosensitive hydrogel-loaded exosomes promote diabetic periodontal bone regeneration through mitochondrial function regulation. *Chem Eng J*. 2025;519:164950. doi:10.1016/j.cej.2025.164950
2. Guo Q, Ren S, Libonati A, et al. Antler stem cell-derived exosomes restore periodontal homeostasis in a rat model with diabetic periodontitis through enhancing ROS scavenging and osteogenesis. *Cell Death Discovery*. 2025;11(1):500. doi:10.1038/s41420-025-02800-6
3. Wang Y, Chu T, Jin T, et al. Cascade reactions catalyzed by gold hybrid nanoparticles generate CO gas against periodontitis in diabetes. *Adv Sci*. 2024;11(24):2308587. doi:10.1002/advs.202308587
4. Qu Y, Zeng H, Wang L, Ge Z, Liu B, Fan Z. Microenvironment-regulated dual-layer microneedle patch for promoting periodontal soft and hard tissue regeneration in diabetic periodontitis. *Adv Funct Mater*. 2025;35(19):2418076. doi:10.1002/adfm.202418076
5. Fan L, Wang T, Liu Y, et al. Natural polyphenol-functionalized schwann cell-derived exosomes as a temporal neuromodulation strategy for diabetic periodontitis therapy. *ACS Nano*. 2025;19(36):32482–32498. doi:10.1021/acsnano.5c08885
6. Pang Y, Kong L, Li Y, et al. PLGA/HA sustained-release system loaded with liraglutide for the treatment of diabetic periodontitis through inhibition of necroptosis. *Mater Today Bio*. 2025;31:101582. doi:10.1016/j.mtbio.2025.101582
7. Yan Y, Li Y, Yang Z, et al. Advanced injectable Ti_3C_2 MXene hydrogel: a multifunctional solution for diabetic alveolar bone defect repair. *Chem Eng J*. 2026;527:171850. doi:10.1016/j.cej.2025.171850
8. Wang C, Li T, Zeng X, et al. Sustained delivery of IL-10 by self-assembling peptide hydrogel to reprogram macrophages and promote diabetic alveolar bone defect healing. *Dent Mater*. 2023;39(4):418–429. doi:10.1016/j.dental.2023.03.014
9. Ye B, Xiang R, Luo F. Hydrogel-Based drug delivery systems for diabetes bone defects. *Chem Eng J*. 2024;497:154436. doi:10.1016/j.cej.2024.154436
10. Lu X, Hu S, Zhang Z, et al. A pH-sensitive CuHP composite hydrogel featuring antibacterial, antioxidant and osteogenic properties for treating diabetic periodontitis. *Regener Biomater*. 2025;12:rbaf065. doi:10.1093/rb/rbaf065
11. Li L, Qin W, Ye T, et al. Bioactive Zn–V–Si–Ca glass nanoparticle hydrogel microneedles with antimicrobial and antioxidant properties for bone regeneration in diabetic periodontitis. *ACS Nano*. 2025;19(8):7981–7995. doi:10.1021/acsnano.4c15227
12. Tang R, Ren Y, Zhang Y, et al. Glucose-driven transformable complex eliminates biofilm and alleviates inflamm-aging for diabetic periodontitis therapy. *Mater Today Bio*. 2023;20:100678. doi:10.1016/j.mtbio.2023.100678
13. Liao Y, Zhang Z, Zhao Y, et al. Glucose oxidase: an emerging multidimensional treatment option for diabetic wound healing. *Bioact Mater*. 2025;44:131–151. doi:10.1016/j.bioactmat.2024.10.006
14. Liao Y, Zhang Z, Hu W, et al. Glucose-regulating hydrogel for immune modulation and angiogenesis through metabolic reprogramming and LARP7-SIRT1 pathway in infected diabetic wounds. *Biomaterials*. 2025;318:123182. doi:10.1016/j.biomaterials.2025.123182
15. Ma Y, Yang J, Ma Y, et al. Glucose oxidase-immobilized dually-crosslinked nanogels for rapid-responsive insulin delivery. *Adv Healthcare Mater*. 2024;13(32):2402556. doi:10.1002/adhm.202402556
16. Tian M, Cheng W, Yang X, et al. Nanozyme cascade reaction system for diabetic retinopathy therapy via glycometabolism and microenvironment regulation. *J Colloid Interface Sci*. 2026;703:139136. doi:10.1016/j.jcis.2025.139136
17. Deng Y, Ouyang X, Sun J, et al. Rapid sterilisation and diabetic cutaneous regeneration using cascade bio-heterojunctions through glucose oxidase-primed therapy. *Bioact Mater*. 2023;25:748–765. doi:10.1016/j.bioactmat.2022.07.003
18. He S, Lin M, Zheng Q, et al. Glucose oxidase energized osmium with dual-active centers and triple enzyme activities for infected diabetic wound management. *Adv Healthcare Mater*. 2024;13(16):2303548. doi:10.1002/adhm.202303548
19. Duan D, Liu S, Xiao T, et al. Self-sacrificial bioenzyme-reinforced injectable hydrogel bone adhesives for enhancing diabetic fracture healing. *Chem Eng J*. 2025;506:160255. doi:10.1016/j.cej.2025.160255
20. Lv N, Sun H, Tang W, et al. A smart bio-battery facilitates diabetic bone defect repair via inducing macrophage reprogramming and synergistically modulating bone remodeling coupling. *Adv Funct Mater*. 2025:e15820. doi:10.1002/adfm.202515820
21. Ma Y, Xie C, Liao C, et al. Zinc-coordinated trienzyme nanogel cascade therapy for accelerated post-pancreatectomy cutaneous wound healing. *Adv Mater*. 2025;37(50):e08538. doi:10.1002/adma.202508538
22. Zheng Y, Mao L, Wang Q, et al. Mitochondria-targeted ROS scavenging natural enzyme cascade nanogels for periodontitis treatment via hypoxia alleviation and immunomodulation. *Adv Sci*. 2025;12(29):e07481. doi:10.1002/advs.202507481

23. Liu W, Shi E, Wu H, et al. Spatially axial boron coordinated single-atom nanozymes with boosted multi-enzymatic performances for periodontitis treatment. *Adv Funct Mater*. 2024;34(39):2403386. doi:10.1002/adfm.202403386
24. Hosseini Hooshiar M, Badkoobeh A, Kolahdouz S, et al. The potential use of nanozymes as an antibacterial agents in oral infection, periodontitis, and peri-implantitis. *J Nanobiotechnol*. 2024;22(1):207. doi:10.1186/s12951-024-02472-x
25. Gao F, Sun M, Zhang J, et al. Fenton-like reaction and glutathione depletion by chiral manganese dioxide nanoparticles for enhanced chemodynamic therapy and chemotherapy. *J Colloid Interface Sci*. 2022;616:369–378. doi:10.1016/j.jcis.2022.02.060
26. Zou H, Hong Y, Xu B, et al. Multifunctional cerium oxide nanozyme for synergistic dry eye disease therapy. *ACS Appl Mater Interfaces*. 2024;16(27):34757–34771. doi:10.1021/acsami.4c07390
27. Lan Z, Han Y, Li J, et al. Cascaded nanozyme-based Fe3O4-GOx@ZIF-8/Ag Janus nanomotors with pH-responsive for photo-Fenton degradation of tetracycline hydrochloride. *J Colloid Interface Sci*. 2026;704:139392. doi:10.1016/j.jcis.2025.139392
28. Zhang Y, Zhang L, Wang M, Li P. The applications of nanozymes in neurological diseases: from mechanism to design. Review. *Theranostics*. 2023;13(8):2492–2514. doi:10.7150/thno.83370
29. Wang Y, Chen C, He C, et al. Quaternized chitosan-based biomimetic nanozyme hydrogels with ROS scavenging, oxygen generating, and antibacterial capabilities for diabetic wound repair. *Carbohydr Polym*. 2025;348:122865. doi:10.1016/j.carbpol.2024.122865
30. Jia M, Ren W, Liu Y, et al. Messenger nanozyme for reprogramming the microenvironment of rheumatoid arthritis. *ACS Appl Mater Interfaces*. 2023;15(1):338–353. doi:10.1021/acsami.2c16458
31. Chen R, Su Y, Zhao G, et al. Nanozyme-integrated hydrogel targeting AGEs for diabetic osteoarthritis therapy. *Adv Sci*. 2025;13(8):e16389. doi:10.1002/advs.202516389
32. Chiam S-L, Pung S-Y, Yeoh FY, Ahmadipour M. Highly efficient oxidative degradation of organic dyes by manganese dioxide nanoflowers. *Mater Chem Phys*. 2022;280:125848. doi:10.1016/j.matchemphys.2022.125848
33. Li H-X, Zhang Q-Y, Sheng N, et al. Mg-EGCG modified multifunctional methacrylated small intestinal submucosa scaffold for enhanced bone regeneration. *J Mater Sci Technol*. 2026;245:182–196. doi:10.1016/j.jmst.2025.03.107
34. Hua S, Zhang Y, Zhu Y, et al. Tunicate cellulose nanocrystals strengthened injectable stretchable hydrogel as multi-responsive enhanced antibacterial wound dressing for promoting diabetic wound healing. *Carbohydr Polym*. 2024;343:122426. doi:10.1016/j.carbpol.2024.122426
35. He Z, Sun C, Ma Y, et al. Rejuvenating aged bone repair through multihierarchy reactive oxygen species-regulated hydrogel. *Adv Mater*. 2024;36(9):2306552. doi:10.1002/adma.202306552
36. Zhang Y, Song Q, Yang S, et al. Revitalizing osteoporotic bone repair via multilevel ROS scavenging and osteoimmune regulating hydrogel. *Composites Part B*. 2025;297:112305. doi:10.1016/j.compositesb.2025.112305
37. Lai W, Zhang L, Liang Y, Zhang G, Zou J, Fei P. Carboxyethyl chitosan/oxidized sodium alginate composite hydrogel loaded with AgNPs and Zn2+: dye adsorption and antibacterial function. *Int J Biol Macromol*. 2025;309:143124. doi:10.1016/j.ijbiomac.2025.143124
38. Yang Z, Wang C, Zhang Z, et al. A pH responsive tannic acid/quaternized carboxymethyl chitosan/oxidized sodium alginate hydrogels for accelerated diabetic wound healing and real-time monitoring. *Int J Biol Macromol*. 2024;264:130741. doi:10.1016/j.ijbiomac.2024.130741
39. Koshy JT, Sangeetha D. Minocycline Hydrochloride-infused Polyvinyl alcohol/ pectin-based bio-nanocomposite antibacterial hydrogel films reinforced with nanofibrillar cellulose from biomass for preventing bactericidal infections in wound dressings. *Carbohydr Polym Technol Appl*. 2025;10:100831. doi:10.1016/j.carpta.2025.100831
40. Huang Y, Fu Z, Wang H, et al. Calcium peroxide-based hydrogels enable biphasic release of hydrogen peroxide for infected wound healing. *Adv Sci*. 2024;11(40):2404813. doi:10.1002/advs.202404813
41. Xu N, Gao Y, Li Z, et al. Immunoregulatory hydrogel decorated with tannic acid/ferric ion accelerates diabetic wound healing via regulating macrophage polarization. *Chem Eng J*. 2023;466:143173. doi:10.1016/j.cej.2023.143173
42. Cheng D, Ding R, Jin X, et al. Strontium ion-functionalized nano-hydroxyapatite/chitosan composite microspheres promote osteogenesis and angiogenesis for bone regeneration. *ACS Appl Mater Interfaces*. 2023;15(16):19951–19965. doi:10.1021/acsami.3c00655
43. Kuang Z, Xiao K, Hu J, et al. Strontium/fluoride surface functionalization engineering of titanium implants with sequential enhanced antibacterial and osteogenesis activities. *Mater Des*. 2025;258:114578. doi:10.1016/j.matdes.2025.114578
44. He Z, Bai X, Xie F, et al. Co-treatment with rhBMP-2 and rapamycin modulates osteogenesis–adipogenesis balance to enhance aged bone regeneration. *Adv Sci*. 2026;13(13):e21619. doi:10.1002/advs.202521619
45. Choi H-Y, Kim H-J, Lee J-Y, Joo J-Y. Adjunctive treatment effect of non-thermal atmospheric pressure plasma in periodontitis-induced rats. *J Clin Med*. 2025;14(3):896. doi:10.3390/jcm14030896